Journal of Asian Earth Sciences xxx (xxxx) xxx–xxx

Contents lists available at ScienceDirect

Journal of Asian Earth Sciences

journal homepage: www.elsevier.com/locate/jseaes

Zircon U–Pb–Hf–O and molybdenite Re–Os isotopic constraints on porphyry gold mineralization in the Bilihe deposit, NE China

Mingtian Zhu[a,b,c,d,e,*], Ke Huang[a,b,c], Lei Hu[f], Yang Bai[a,b,c], Wenjun Li[a,b], Bingyu Gao[a,b], Lianchang Zhang[a,b,c]

[a] Key Laboratory of Mineral Resources, Institute of Geology and Geophysics, Chinese Academy of Sciences, Beijing 100029, China
[b] Institutions of Earth Science, Chinese Academy of Sciences, Beijing 100029, China
[c] University of Chinese Academy of Sciences, Beijing 100049, China
[d] Institute of Earth Science and Engineering, Shandong University of Science and Technology, Qingdao 266510, China
[e] State Key Laboratory of Ore Deposit Geochemistry, Institute of Geochemistry, Chinese Academy of Sciences, Guiyang 550081, China
[f] Shandong Institute of Geophysical and Geochemical Exploration, Jinan 250013, China

ARTICLE INFO

Keywords:
Geochronology
Hf–O isotopes
Bilihe deposit
Porphyry gold deposit
CAMD

ABSTRACT

The Bilihe gold deposit in Inner Mongolia is situated in the Central Asian Metallogenic Domain. Its major orebody II is a porphyry-type body, spatially and temporally associated with granodiorite porphyry and granite aplite. In this study, the timing of gold mineralization is precisely constrained by using the zircon U–Pb dating for pre-mineralization intrusions and the molybdenite Re–Os dating for later molybdenite veins. Furthermore, zircon Hf–O isotope analyses have also been carried out to decipher the nature of primary magma. Zircon U–Pb dating shows that the granodiorite porphyry and the granite aplite were emplaced at 269 ± 2 Ma and 270 ± 2 Ma, respectively, indicating the gold mineralization occurring no earlier than 269 Ma. Meanwhile, molybdenite veins are developed within the fractures and commonly cut across the auriferous veins. Thus, combined with a molybdenite Re–Os isochron age of 268 ± 1 Ma, the gold mineralization in the Bilihe deposit can be precisely restricted to ca. 269 Ma. Zircon ε_{Hf} (t) values are mostly positive (1.6–11.3), along with high $\delta^{18}O$ values of 6.20–7.63‰, suggesting a mixed source between mantle materials and ancient continental crust (such as the Bainaimiao Group) for the Bilihe magma. It is also supported by the presence of the captured detrital zircons in these intrusions. Given a universally metallogenic environment for porphyry gold deposits, a thicken crustal setting related to the collisional intermission of the Paleo-Asian Ocean is favored to interpret the formation setting of the Bilihe deposit.

1. Introduction

The porphyry gold-only deposit represents a relatively new type of economic gold ore devoid of economically mineable copper and molybdenum and is commonly formed in subduction-related volcano-plutonic arcs (Sillitoe, 1979; Sillitoe, 2010). So far, only tens of porphyry gold deposit have been found and reported worldwide (Fig. 1), e.g., the Marte, Verde and Pancho deposits in the Maricunga Belt, Chile (Vila et al., 1991; Muntean and Einaudi, 2000), the Colosa and Marmato deposits in the Middle Cauca belt in Columbia (Sillitoe, 2008; Gil-Rodríguez, 2010), the Biely Vrch deposit in the Javorie belt in Slovakia (Hanes et al., 2010) and the Bilihe deposit in China (Ge et al., 2009). Compared with the porphyry Cu ± Au ± Mo deposit, the type of deposit is characterized by (1) ore-forming paleo-depth of less than 1 km, (2) genetically related subvolcanic porphyry that is commonly covered by coeval volcanic rocks, (3) extremely low content of sulfides (2 wt%) but relatively higher content of oxides (5 wt%), (4) gold ore spatially associated with chlorite-magnetite-albite alteration, (5) the presence of gold dominantly within banded quartz-magnetite veinlets, and (6) gold precipitation in a high-temperature but low-pressure subvolcanic setting. Considering its mineralization model, Sillitoe (1979) argued an island arc magmas with higher oxygen fugacity tending to be rich in gold and poor in molybdenum; Muntean and Einaudi (2000) emphasized shallow episodic intrusion that permits loss of sulfur and precipitation of gold-rich banded quartz veinlets, whereas Richards (2009) favored partial melting of an exceptional magma reservoir characterized by hydrous, Au-rich, but relatively sulfur-poor magmas. In addition, Koděra et al. (2014) proposed a K-Fe-enriched

* Corresponding author at: Key Laboratory of Mineral Resources, Institute of Geology and Geophysics, Chinese Academy of Sciences, Beijing 100029, China.
E-mail address: junrich@mail.iggcas.ac.cn (M. Zhu).

https://doi.org/10.1016/j.jseaes.2018.07.016
Received 7 September 2017; Received in revised form 11 July 2018; Accepted 12 July 2018

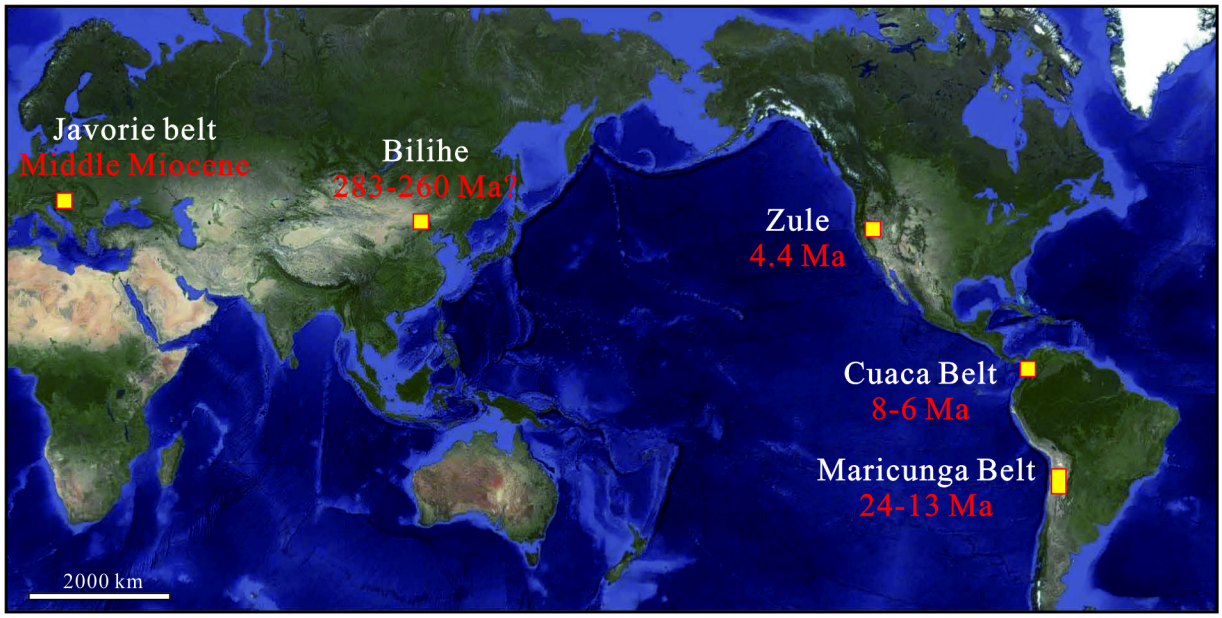

Fig. 1. Porphyry gold distribution around the world. See text for detailed sources of the age data.

mantle-derived magmatic fluid responsible for the formation of the Biely Vrch gold deposit in Slovakia.

Currently known porphyry gold deposits are mostly formed after the Miocene (Fig. 1). In northern Chile, the Maricunga belt hosts porphyry Au deposits of two discrete periods of 24–21 Ma and 14–11 Ma, which are closely associated with fine-grained diorite to quartz diorite porphyry stocks emplaced into andesitic stratovolcanoes (Sillitoe et al., 1991; Muntean and Einaudi, 2001; Gamonal, 2015). In Colombia, the andesite to dacite rocks in the Cauca belt were dated between 6 and 8 Ma, providing significant time constraint on the Colosa and Marmato porphyry Au deposits (Sillitoe, 2008; Santacruz Reyes, 2016). In the western European Carpathian Mountains, the Javorie belt in Slovakia owns several occurrences of porphyry gold mineralization and an economic ore at Biely Vrch. There are hosted within the stocks of Middle

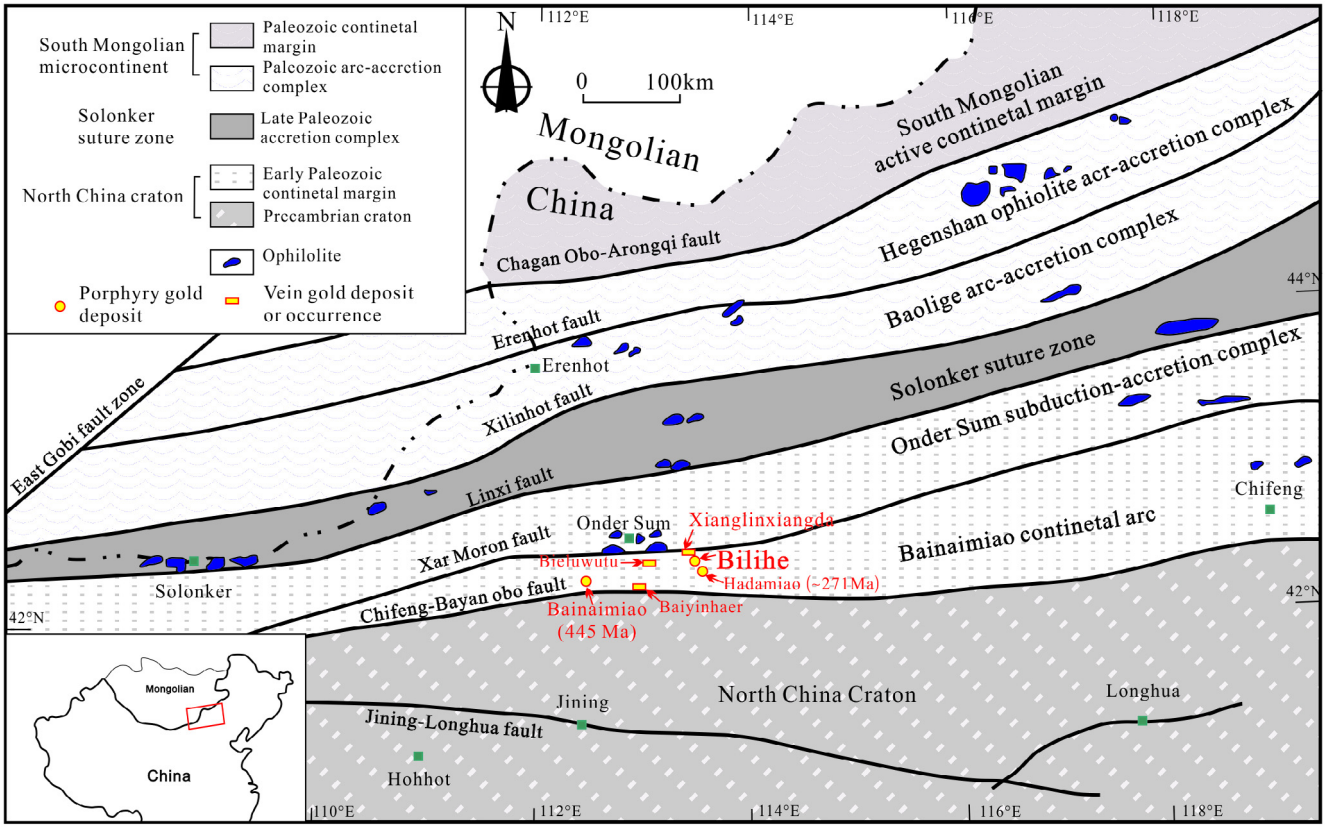

Fig. 2. Tectonic map of central Inner Mongolia showing the tectonic belts and the Au-bearing distribution in the study area (after Xiao et al., 2003). Isotopic ages of the gold deposits are from Lu et al. (2009), Li et al. (2012) and Liu et al. (2014).

Miocene diorite-to-granodiorite porphyry (Szabó et al., 1992; Hanes et al., 2010; Koděra et al., 2014).

In China, the Bilihe gold deposit in Inner Mongolia located in the Central Asian Orogenic Belt (CAOB) is considered as the known oldest porphyry gold deposit, although Yang et al. (2016) defined it as a new type of Au deposit of magmatic origin based on its wide distribution of high-temperature dendritic and comb-layered quartz. The Bilihe deposit represents an epithermal-porphyry system, consisting mainly of two orebodies, that are the epithermal orebody I with 3.1 t Au which has been mined out and the newly discovered porphyry orebody II with 21.6 t Au (Ge et al., 2009). Previous geochronological works indicate that it was formed at the Permian and gave very discrete time ranges. Lu et al. (2012) considered that the porphyry related to the orebody II was formed 284 ± 4 Ma, whereas Yang et al. (2016) obtained a zircon U–Pb age of 261 ± 2 Ma. Liu and Nie (2015) argued that the magmatic and hydrothermal activities lasted for ca. 17 Ma from 272 Ma to 255 Ma using ages of the peripheral intrusions of the orebody II. In addition, Qing et al. (2011) applied 250–273 Ma molybdenite model Re–Os ages from the orebody II to constrain the gold mineralization at 273 Ma. In this paper, on the basis of occurrences of ore-related porphyry and molybdenite selected from later hydrothermal veins, we present TIMS-1280 zircon U–Pb and molybdenite Re–Os isotopic analyses to confine the timing of the porphyry orebody II and use *in situ* zircon Hf–O isotopes to trace the magma source and to discuss the relationship between the evolution of the Paleo-Asian ocean and the gold mineralization.

2. Regional geology

CAOB is one of the largest accretionary orogens on the earth (Şengör et al., 1993; Windley et al., 2007); it is terminated by the Solonker

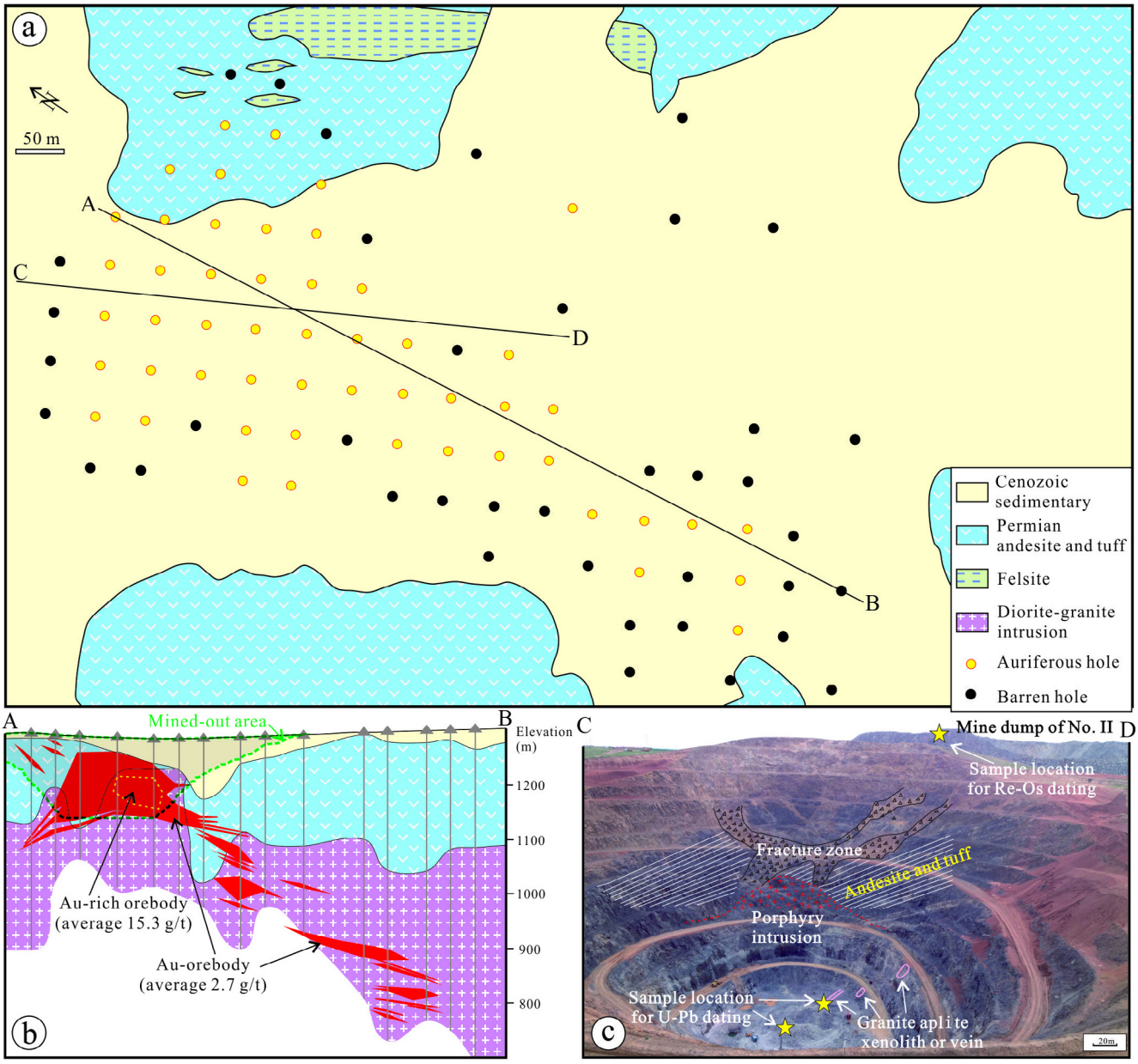

Fig. 3. a – Geological map of the porphyry II buried orebody in the Bilihe gold deposit (Ge et al., 2009). b – Northwest-southeast cross-section showing the locations of Au-rich and Au-poor orebodies and of the mined-out area. c – Picture of the open pit showing the relationship between the porphyry intrusion and andesite tuff and sampling locations for this study.

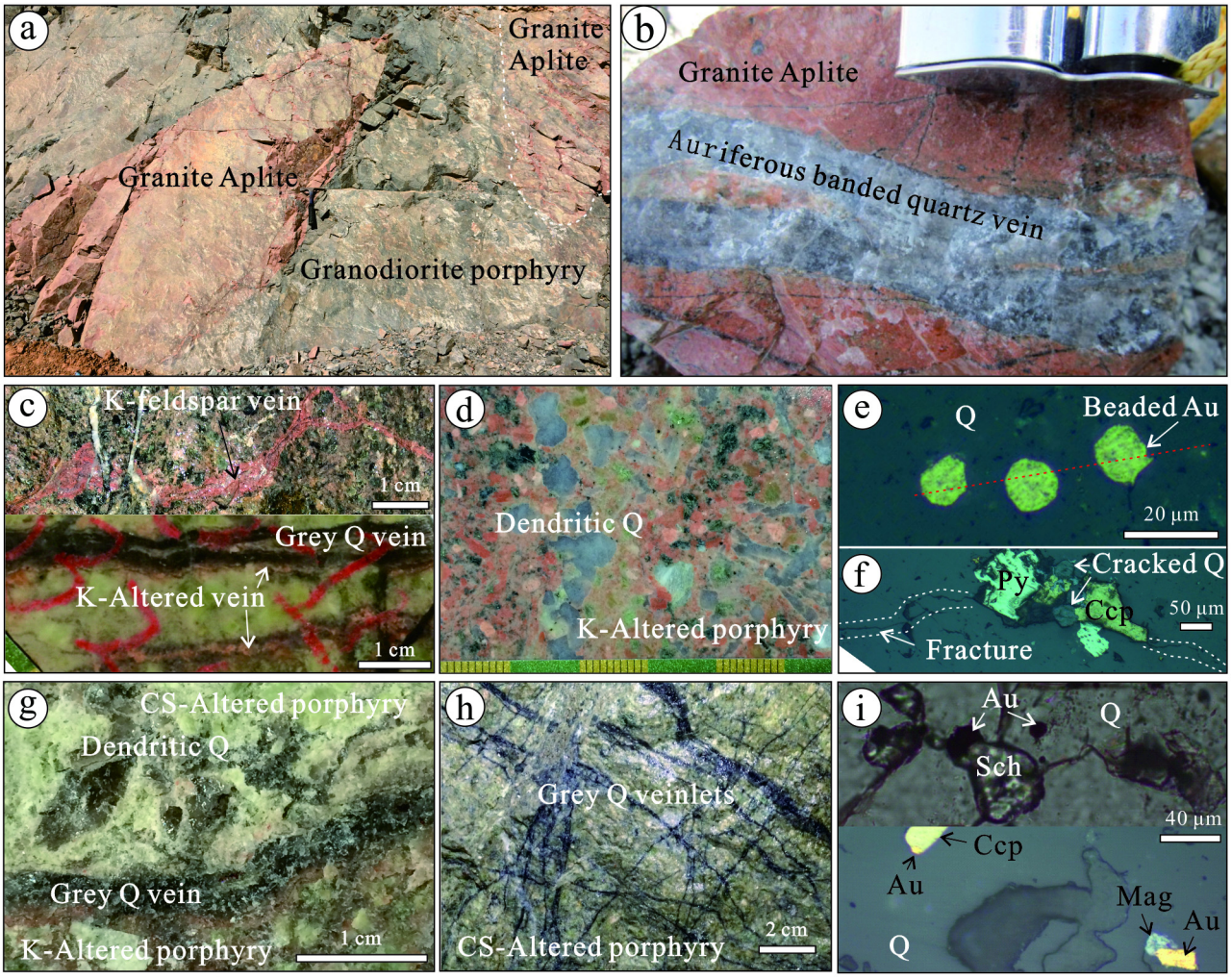

Fig. 4. Photographs showing the occurrences of intrusions and auriferous quartz. a – Granite aplites show flat boundaries with granodiorite porphyry; b – Auriferous quartz veins cut through an aplite along extensional fractures; c – K-feldspar veins are distributed in the porphyry (upper part) and cracked by gray quartz (Q) veins in the strongly altered porphyry (lower part); d – Dendritic quartz occurs in potassium (K-) alteration porphyry; e – Au grains cluster as droplet shapes in the dendritic quartz; f – Chalcopyrite (Ccp) and pyrite (Py) are distributed along fractures in dendritic quartz, and the quartz was cracked into globular shapes when the fractures cut through; g – Dendritic quartz is enclosed in chlorite-sericite (CS-) altered porphyry, and chlorite-sericite and potassium alterations are divided by gray auriferous quartz veins; h – Auriferous gray banded quartz veinlets are injected into CS altered porphyry; i – Coexisting Au, scheelite, magnetite (Mag) and chalcopyrite in grey quartz.

suture between the southern North China Craton and the northern Siberian Craton (Xiao et al., 2003). The Bilihe deposit tectonically belongs to the southern accretionary zone between the North China Craton and the Solonker suture. This zone is composed of the Middle-Ordovician-Early Silurian Ondor Sum subduction-accretion complex and the Bainaimiao arc (Fig. 1; Xiao et al., 2003). The Bainaimiao arc, hosting the Bilihe deposit, used to be considered as an island arc (Tang and Yan, 1993), and was recently regarded as a subduction-related continental margin arc, with the Mesoproterozoic Bainaimiao Group consisting of two-mica schists and biotite-plagioclase schists (Nie et al., 1995; Xiao et al., 2003). In the Late Silurian, southward subduction resulted in a collision between the Bainaimiao arc and the North China Craton bounded by the Chifeng-Bayan Obo fault (Xiao et al., 2003; Li et al., 2009). The southern accretionary zone was finally consolidated by the Carboniferous-Permian or even the Triassic, when it evolved into an Andean-type magmatic margin above a south-dipping subduction zone along the northern Solonker fault (Xiao et al., 2003; Zhang et al., 2009a). Accordingly, the CAOB has experienced crustal evolution that involved both juvenile material and abundant reworking of older crust with varying proportions in the Paleozoic generation of the arc terranes in Inner Mongolia (Kröner et al., 2014).

Several porphyry Cu–Au deposits and lode gold deposits are developed in the Bainaimiao arc, e.g., the Bainaimiao Cu–Au deposit, the Hadamiao Au deposit and the Bilihe Au deposit (Fig. 2). The Bainaimiao Cu–Au deposit and related porphyry intrusions were intensely reworked by later EW-trending shear zones. Li et al. (2012) obtained similar zircon U–Pb and molybdenite Re–Os ages of 445 Ma for the ore-related porphyry and Cu–Au mineralization, respectively, and interpreted the Bainaimiao deposit as a Late Ordovician porphyry system that has undergone intense deformation and metamorphism in the Middle Devonian (Nie et al., 1994b). The Hadamiao Au deposit is 12 km southeast of Bilihe and related to a 272 Ma granitic intrusion (Lu et al., 2009; Liu et al., 2014). Given similar geological features between the Hadamiao and Bilihe deposits Yang et al. (2016) further argued that

these two belonged to one district. The Baiyinhaer lode Au deposit occurs within the 427 Ma quartz diorite (our unpublished data), and Xianglinxiangda and Bieluwutu lode gold deposits are genetically associated the Late Permian quartz diorite and 275 Ma volcanics, respectively (our unpublished data; Nie et al., 1994a). Clearly, at least two periods of gold mineralization occurred in the Bainaimiao arc related with Ordovician–Silurian and Permian magmatic events.

3. Deposit geology

The Bilihe deposit is situated in the Durewuligi volcanic basin. Outcropping strata are mainly of Permian volcanic sedimentary rocks and overlying Cenozoic sedimentary rocks. These volcanic sequences were considered to be deposited in the Jurassic. However, detailed zircon U–Pb dating for andesitic rocks (281 ± 4 Ma) and rhyolite (273 ± 3 Ma) in the Bilihe district indicates that the volcanics erupted in the Permian; (Qin et al., 2012; Yang et al., 2016). The NW-trending extensional faults, as secondary branches of regional deep faults, control the distribution of intrusions, whereas the NE-trending faults were interpreted as post-mineralization with large effects on the gold orebody (Lu et al., 2009). The Bilihe deposit is composed of the porphyry orebody II and vein orebodies of I and 22–26. The latter vein mineralization occurs in the andesite or tectonic breccia related with deeper porphyry (Ge et al., 2009). Exposed intrusions in the south of the orebody II and the hidden intrusions below the orebody 22 have been studied in detail by Liu and Nie (2015), who considered that these 255–271 Ma intrusions are generally high-K calc-alkaline, sourced from mixing among the partial melting of subducted oceanic crust, depleted mantle and lower crust in a collisional to extensional setting during the late stage of closure of the Paleo-Asian Ocean.

The porphyry orebody II was overlain by andesite, tuff and Cenozoic sedimentary rocks (Fig. 3). At the surface, andesite outcrops underwent intense oxidation and were cut by discontinuous quartz veins. The contact zone between the intrusion and andesitic lava is filled with the breccia (Fig. 3c). The gold orebody is spatially and temporally associated with porphyry intrusions (Fig. 3b), with geochemical compositions changing from diorite in the lower part to granite in the upper part (Yang et al., 2016). Additionally, the granite aplite dikes or fragments are also present in the orebody II. The aplites are usually several to tens of meters long (Fig. 4a), showing apparently unaltered boundaries with the porphyry and possibly representing the fractionated product of the porphyry. Auriferous banded quartz veins commonly crosscut the aplites and porphyry along extensional fractures (Fig. 4b).

Overall, the gold orebody dips SE (Fig. 3b), indicating the upwelling direction of the hydrothermal fluid. Quartz as the dominant mineral has very different occurrences, including dendritic, agglomerated and vein shapes. The former two probably represent a physical model of hydrothermal exsolution from magma (Harris et al., 2004) or quartz phenocryst phases in magma (Yang et al., 2015). The sulfides are rare (less 2%) and consist mainly of pyrite, chalcopyrite, molybdenite, bornite, sphalerite and galena, whereas oxides account for ~5%, and are composed mainly of magnetite and ilmenite. Magnetite is found both in the porphyry and the hydrothermal veins, whereas the ilmenite commonly occurs either mineral inclusions in pyroxene and plagioclase or intergrowth with magnetite. The gold grains have different shapes with approximately 11% of gold grains occurring as droplets or round shapes and the rest as irregular or angular shapes (Bai and Qin, 2012). Pervasive alterations include early potassic alteration and late superposed chlorite-sericite-illite, sericite-quartz-pyrite and advanced argillic alterations, resulting in remnant potassic alteration found only at depth. Tourmalinization is common in the intrusions and wall rocks, indicating intensive magma degassing.

Based on gold occurrences and grades, two types of gold mineralization can be distinguished (Fig. 3b). One type is Au-rich orebody (ca. 8 t Au) with an average grade of 15.0 g/t (Bai and Qin, 2012), occurring in a top “cap” section of the porphyry intrusion. This “gold core” is genetically related with coarse-grained and dendritic quartz and is almost mined out in an open pit (Fig. 3b and c). In the shallow part, dendritic quartz is present in envelopes of sericitization and kaolinization, whereas in the deep part, it can be found in potassic alteration zones (Fig. 4c and d). These quartz grains have irregular curving shapes and host droplet-shaped gold grains (Fig. 4e). Most Au grains are native, euhedral or subhedral and cluster as beaded trails along intersecting crystallographic planes of the hosted quartz, indicating simultaneous precipitation with quartz (Yang et al., 2015). Rare sulfides are distributed in the dendritic quartz, and only pyrite and chalcopyrite can be found along the fractures (Fig. 4f). The other type is gray banded quartz veinlets with an average Au grade of 2.7 g/t (Bai and Qin, 2012), occurring in the intrusions and andesitic wall rocks and overprinting the dendritic quartz (Fig. 4g and h). This gold mineralization is mainly associated with chlorite-sericite-illite alteration and is thus later than the potassium alteration (Fig. 4c, g and h). The gold commonly coexists with scheelite, magnetite and chalcopyrite (Fig. 4i), indicating an intense redox transitional environment for gold precipitation.

4. Samples and analytical methods

Granodiorite porphyry and granite aplite samples for zircon U–Pb and Hf–O analyses were chosen from ca. −1140 m in the open pit (Fig. 3c). Zircon grains were separated via a combination of heavy liquid and magnetic techniques, handpicked, and then mounted in epoxy resin and polished to remove the upper one-third of the grains. The mount was vacuum-coated with high-purity gold prior to SIMS analysis. Cathodoluminescence (CL) and back-scattered electron (BSE) images were obtained based on a LEO1450 VP SEM in order to identify internal structures and inclusions, and choose potential target sites for U–Pb analysis. Zircon U–Pb–O analyses were carried out on the Cameca IMS-

Table 1
Sample information of molybdenite.

Sample	Occurance (mine dump of No. II orebody)		
	host rock	molybdente shape	mineral association
B-Mo-101	weak-altered granodiorite porphyry	thin film in fracture	molybdenite
B-Mo-06	light-green altered granodiorite porphyry	disseminated in quatz veinlet	molybdenite + quartz + pyrite;
B-Mo-06-1	hornfelsed tuff sandstone	thin film in fracture	molybdenite
B-Mo-08	light-green altered granodiorite porphyry	thin film in fracture	molybdenite
B-Mo-401	light-green altered granodiorite porphyry	cloddy in quatz-carbonate veinlet	molybdenite + quartz + calcopyrite ± pyrite + calcite
B-Mo-402	light-green altered granodiorite porphyry	cloddy in quatz-carbonate veinlet	molybdenite + quartz + calcopyrite ± pyrite + calcite
B-Mo-403	light-green altered granodiorite porphyry	cloddy in quatz-carbonate veinlet	molybdenite + quartz + calcopyrite ± pyrite + calcite
B-Mo-404	light-green altered granodiorite porphyry	cloddy in quatz-carbonate veinlet	molybdenite + quartz + calcopyrite ± pyrite + calcite
B-Mo-405	light-green altered granodiorite porphyry	cloddy in quatz-carbonate veinlet	molybdenite + quartz + calcopyrite ± pyrite + calcite

1280 large-radius SIMS at the Institute of Geology and Geophysics, Chinese Academy of Sciences (IGGCAS). The detailed analytical procedures can be found in Li et al. (2010a). The ^{204}Pb and ^{207}Pb correction methods were used for individual analyses, and an average ^{206}Pb/^{238}U age with 2 σ or 95% confidence level was calculated using ISOPLOT 3.0 (Ludwig, 2003). To monitor the external uncertainties of SIMS U–Pb zircon dating calibrated against the Plesovice standard, an in-house zircon standard Qinghu was alternately analyzed as an unknown together with other unknown zircons. Nine measurements on the Qinghu zircon yielded a concordia age of 160 ± 1 Ma, which was identical within error to the recommended value of 159.5 ± 0.2 Ma (Li et al., 2013). Measured ^{18}O/^{16}O values were normalized to the Vienna Standard Mean Ocean Water composition (VSMOW, ^{18}O/^{16}O = 0.0020052). The instrumental mass fractionation factor (IMF) was corrected using the Penglai zircon standard with a δ^{18}O value of 5.3‰. A second zircon standard Qinghu was analyzed as an unknown to ascertain the veracity of the IMF. Nineteen measurements of the Qinghu zircon yielded a weighted mean δ^{18}O of 5.4 ± 0.2‰, consistent with the reported value of 5.4 ± 0.2‰ (Li et al., 2013). Zircon Hf isotopic measurements were carried out *in situ* using a Neptune MC-ICP-MS equipped with a 193 nm ArF excimer laser ablation system at IGGCAS. Detailed analytical procedures were described in Wu et al. (2006). The zircon Mud Tank was used as a standard reference material during routine analyses; its weighted mean ^{176}Hf/^{177}Hf ratio of 0.282507 ± 26(2 SD, n = 14) was indistinguishable from that obtained by Woodhead et al. (2004) (^{176}Hf/^{177}Hf = 0.282507 ± 6); A second zircon standard Penglai was analyzed as an unknown sample yielding a ^{176}Hf/^{177}Hf ratio of 0.282915 ± 21 (2 SD, n = 7), consistent with the reported value of 0.282906 ± 0.0000010 within error (Li et al., 2010b). The Hf–O analyses for the zircons were obtained using the same mounts as used for U–Pb dating. Generally, if the grain was large enough, we ran the Hf–O analyses near the U–Pb spot; otherwise, on top of the U–Pb site.

Nine molybdenite samples for Re–Os analysis were selected from the mine dump of the orebody II. Molybdenite occurs in fractures or quartz veins within various host rocks, from hornfels tuff sandstone to granite aplite and weakly–strongly altered granodiorite (Table 1). Molybdenite veins obviously cut the agglomerated and vein quartz (Fig. 5), reflecting a later forming feature than the gold mineralization. When controlled by fractures, molybdenite usually develops by itself, but when it occurs in hydrothermal veins, associated minerals are composed mainly of quartz and calcite, with minor chalcopyrite and pyrite (Fig. 5). Molybdenite mineral separates were produced by rough crushing and subsequent handpicking, approximately 40–60 mesh size fraction. All Re–Os chemistry and analyses were performed at the Re–Os Laboratory in the Key Laboratory of Mineral Resources, IGGCAS. The details of the chemistry and measurement procedure are described by Jin et al. (2010) and Jin et al. (2013).

5. Results

5.1. Zircon U–Pb dating

Most zircons in the granodiorite porphyry are relatively integrated, with average diameters of 100 μm. They also show typical oscillatory zoning with variable CL intensity, indicating their magmatic affinity (Fig. 6a). In addition, a few grains have relatively blurry and dark luminescence, suggesting metasomatism, which was also confirmed by

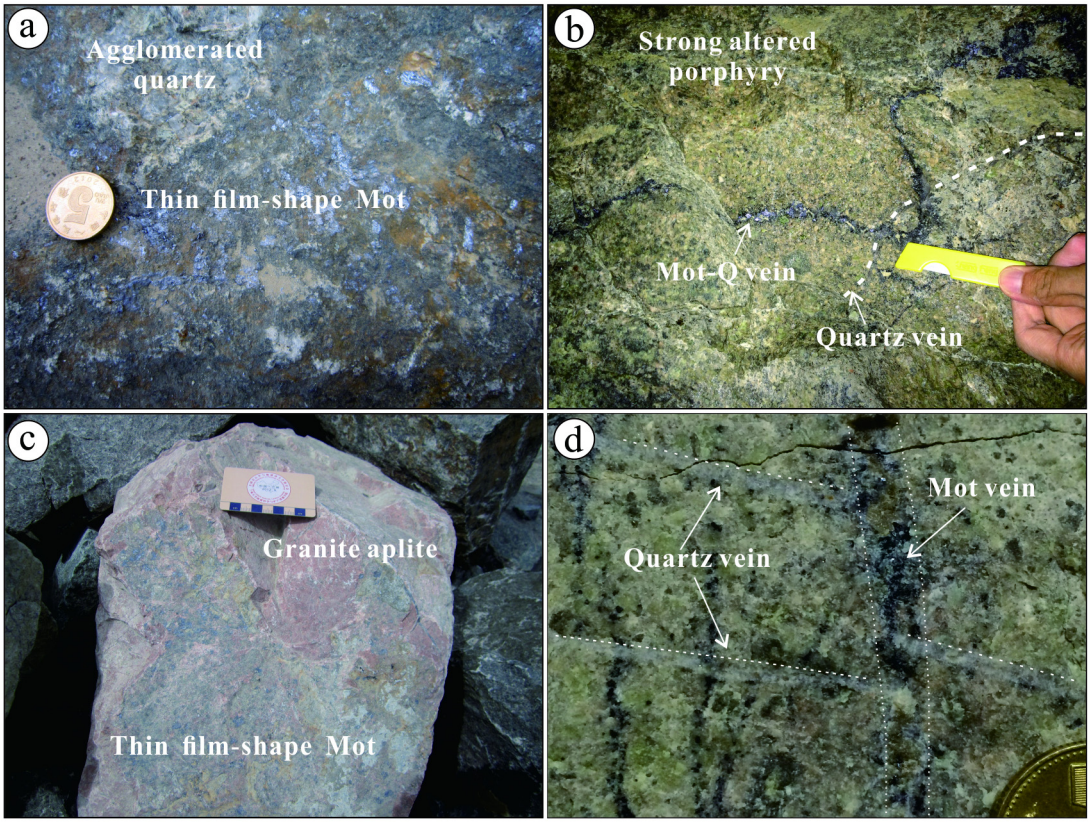

Fig. 5. Molybdenite occurrences in the Bilihe deposit. (a) Thin film-shaped molybdenite (Mot) cuts through agglomerated quartz along with a fracture; (b) Molybdenite–quartz vein cuts off an auriferous quartz vein in light-green strongly altered porphyry; (c) Thin film-shaped molybdenite is distributed in the granite aplite; (d) Molybdenite–quartz vein crosscuts quartz veins. (For interpretation of the references to color in this figure legend, the reader is referred to the web version of this article.)

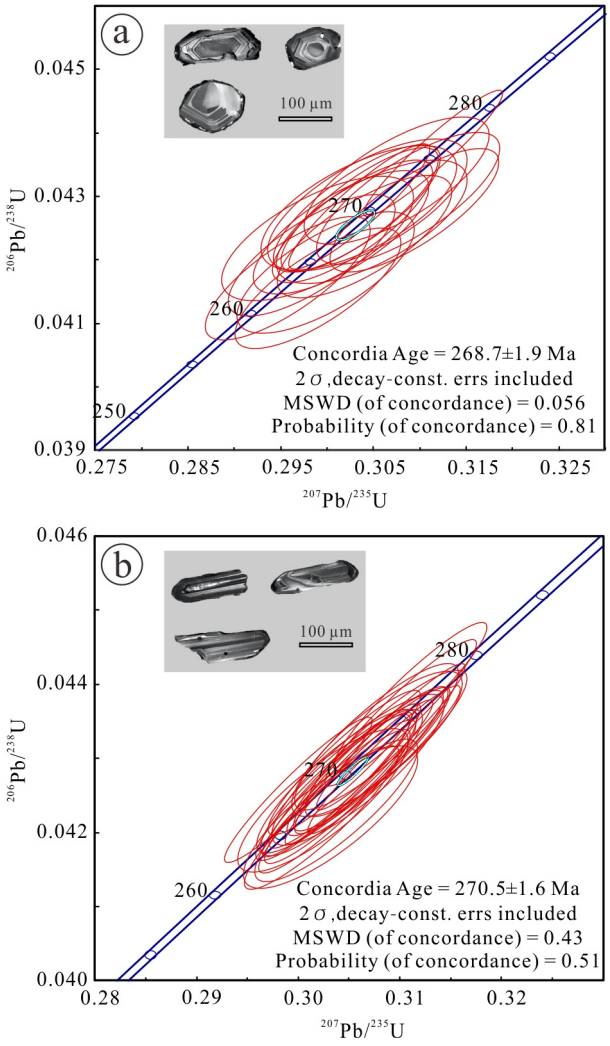

Fig. 6. Zircon U–Pb concordia diagrams for granodiorite porphyry (a) and granite aplite (b).

U–Pb analyses. Zircons in granite aplite share similar features with magmatic grains, showing typical oscillatory zoning (Fig. 6b). The greatest difference compared with the former is the shape; most of the grains are elongated columnar or fragmentary, with aspect ratios of 1:2–1:5.

A total of 23 analyses on 23 grains (Table 2) were determined for granodiorite porphyry. They clustered into two populations on the concordia diagram, although they had indistinguishable Th/U ratios ranging from 0.40 to 1.03. Five zircon grains showing metamorphic CL images define a concordia age of 445 ± 6 Ma (MSWD = 1.3; not shown), representing the age of ancient crustal rocks in this area. The remaining grains yielded relatively concentrated apparent $^{206}Pb/^{238}U$ ages and had variable concentrations of U and Th, ranging from 148 to 655 ppm and 75 to 579 ppm, respectively, with an exception of 1152 ppm and 1190 ppm; Th/U ratios vary from 0.50 to 0.89, with an average ratio of 0.67, with an exception of 1.03. A concordia age of 269 ± 2 Ma (MSWD = 0.4; Fig. 6a) should represent the crystallization time of the granodiorite porphyry, which constrains the upper limit time of gold deposition.

A total of 24 analyses on 24 grains were determined for granite aplite and gave scattered U and Th concentrations of 279–2504 ppm and 114–1318 ppm, respectively, with relatively concentrated Th/U ratios of 0.16–0.55, and almost without Pb loss. A concordia age of 270 ± 2 Ma (MSWD = 0.1; Fig. 6b) should represent the crystallization time of the granite aplite, which is similar to the formation age of the gold-related intrusion within error.

5.2. Zircon Hf–O analyses

Thirty-three *in situ* Hf–O isotope analyses were performed on the same zircon zones as the U–Pb analyses. From the data set in Table 2, 445 Ma zircons from the granodiorite porphyry have lower $^{176}Hf/^{177}Hf$ ratios than 270 Ma grains (0.282451–0.282701 vs. 0.282755–0.282934, respectively), but have no obvious distinction in $^{176}Lu/^{177}Hf$. They all show positive ε_{Hf} values (3.1–6.9 vs. 5.2–11.3, respectively), excepting one 445 Ma grain with a value of -1.9. The calculated Hf model ages (TDM1 and TDM2) for the 445 Ma zircons range from 790 to 1136 Ma and 883–1136 Ma, respectively, and for the 270 Ma ones, from 465 to 694 Ma and 513–823 Ma, respectively. The granodiorite porphyry has higher ε_{Hf} (t) values and younger model ages than the 445 Ma crustal rocks, likely representing their different magma reservoirs. Meanwhile, the granite aplite has relatively concentrated $^{176}Hf/^{177}Hf$ ratios of 0.282651–0.282766, corresponding to positive ε_{Hf} (t) values of 1.6–5.6. The calculated Hf model ages (TDM1 and TDM2) range from 680 to 838 Ma and 803 to 1011 Ma, respectively, similar to the model ages for gold-related intrusions.

The investigation of O isotopes shows that from the 445 Ma captured zircons to the 270 Ma and 269 Ma crystallized ones, $\delta^{18}O$ values have no obvious difference, ranging from 6.20‰ to 7.63‰, which are higher than the modern mantle-like $\delta^{18}O$ value of 5.3 ± 0.6‰ (Valley et al., 1998). A $\delta^{18}O_{zircon}$-rich source should have been involved in the evolution of the ore-forming magma.

5.3. Molybdenite Re–Os analyses

In the field, two occurrences of molybdenite can be recognized, including thin films and coarse grains (Table 3). The former is controlled by fractures in various host rocks, while the latter with a size up to several centimeters is found in hydrothermal quartz veins where sulfides (e.g., chalcopyrite and pyrite) are also present. As shown in Table 3, the contents of Re in thin films molybdenite are obviously lower than those in coarse grains of molybdenite (averages of 1005 ppm vs. 2332 ppm, respectively), and similarly for ^{187}Re and ^{187}Os (averages of 632 ppm vs. 1466 ppm and 2830 ppb vs. 6551 ppb, respectively), indicating a positive relationship between grain size and enrichment in Re and Os. However, they all yield similar model ages from 266 to 271 Ma, with a weighted mean age of 268 ± 1 Ma (Fig. 7). When plotted on the ^{187}Os vs. ^{187}Re correlation diagram, an isochron age of 268 ± 1 Ma can be regressed, with a large error initial ^{187}Os value of 5.1 ± 5.9 (MSWD = 0.58, Fig. 7). Hence, we suggest that 268 Ma best represents the age of molybdenite mineralization, constraining the lower limit time of gold deposition.

6. Discussion

With regard to the genesis of the Bilihe deposit, Yang et al. (2015) emphasized its magmatic origin by means of detailed petrographic observation on gold occurrences and melt inclusions in the dendritic quartz. There is no doubt that this high Au grade “gold core” indeed existed in the orebody II likely related to the high-temperature dendritic quartz, yet it only accounts for nearly one third in terms of the total Au reserve of orebody II, and most of the gold occurs within the hydrothermal banded quartz veins. Additionally, a number of gold grains in the dendritic quartz were found within micro-fracture that only can be recognized under CL image (see Appendix A). Clearly, these

Table 2
Zircon U-Pb and Hf-O results of the Bilihe gold deposit.

Sample No.	Ratio						Model age						U-Th		
	$^{207}Pb/^{206}$-Pb	1σ (%)	$^{207}Pb/^{235}U$	1σ (%)	$^{206}Pb/^{238}U$	1σ (%)	$^{207}Pb/^{206}Pb$	1σ	$^{207}Pb/^{235}$-U	1σ	$^{206}Pb/^{238}$-U	1σ	U (ppm)	Th (ppm)	Th/U
BL1-6 Granodiorite porphyry; Concordia age = 269 ± 2 Ma (MSWD = 0.4)															
BL1-6-1	0.05137	1.22	0.30324	1.96	0.0428	1.53	257.6	27.7	268.9	4.6	270.2	4.1	194	100	0.516
BL1-6-2	0.05219	1.53	0.30433	2.33	0.0429	1.60	262.9	38.6	269.8	5.5	270.6	4.2	225	156	0.696
BL1-6-3	0.05275	1.19	0.30403	2.04	0.0424	1.50	287.7	31.3	269.5	4.8	267.5	3.9	207	159	0.769
BL1-6-4	0.05237	1.41	0.30340	2.29	0.0428	1.50	258.2	39.2	269.1	5.4	270.3	4.0	149	75	0.506
BL1-6-5	0.05192	1.17	0.29830	1.99	0.0421	1.50	259.8	29.8	265.1	4.7	265.7	3.9	220	161	0.730
BL1-6-6	0.05138	0.67	0.30346	1.66	0.0428	1.51	257.8	15.4	269.1	3.9	270.4	4.0	655	579	0.883
BL1-6-7	0.05277	1.25	0.29985	2.11	0.0418	1.50	286.4	33.4	266.3	4.9	264.0	3.9	193	136	0.703
BL1-6-8	0.05190	1.65	0.30479	2.23	0.0426	1.51	280.9	37.2	270.1	5.3	268.9	4.0	261	185	0.710
BL1-6-9	0.05153	1.15	0.30273	1.89	0.0426	1.50	264.7	26.1	268.5	4.5	269.0	4.0	226	166	0.733
BL1-6-10	0.05153	1.42	0.30151	2.07	0.0424	1.51	264.5	32.3	267.6	4.9	267.9	4.0	148	75	0.505
BL1-6-11	0.05226	1.39	0.29897	2.28	0.0423	1.52	250.7	38.8	265.6	5.4	267.3	4.0	207	144	0.693
BL1-6-12	0.05171	0.50	0.31142	1.59	0.0437	1.51	272.7	11.5	275.3	3.8	275.6	4.1	1152	1190	1.034
BL1-6-13	0.05209	1.37	0.30749	2.14	0.0432	1.53	266.1	33.8	272.2	5.1	272.9	4.1	283	251	0.886
BL1-6-14	0.05144	1.08	0.30351	1.85	0.0428	1.51	260.7	24.5	269.1	4.4	270.1	4.0	282	168	0.597
BL1-6-15	0.05245	1.22	0.30940	1.93	0.0428	1.51	305.2	27.5	273.7	4.7	270.0	4.0	196	138	0.701
BL1-6-16	0.05143	1.23	0.29577	1.98	0.0417	1.54	260.0	28.1	263.1	4.6	263.4	4.0	198	135	0.683
BL1-6-17	0.05220	1.28	0.29906	1.97	0.0416	1.50	294.0	29.0	265.7	4.6	262.5	3.9	187	108	0.577
BL1-6-18	0.05212	1.38	0.30876	2.11	0.0430	1.60	290.8	31.2	273.2	5.1	271.2	4.2	157	81	0.514
BL1-6 Core domain; Concordia age = 445 ± 6 Ma (MSWD = 1.3)															
BL1-6-1	0.05633	0.64	0.55684	1.64	0.0720	1.51	455.6	14.5	449.5	6.0	448.3	6.5	411	262	0.636
BL1-6-2	0.05663	0.80	0.56185	1.76	0.0722	1.55	470.0	18.3	452.7	6.4	449.3	6.7	252	235	0.933
BL1-6-3	0.05619	0.78	0.53974	1.70	0.0698	1.50	454.3	17.7	438.3	6.1	435.2	6.3	276	183	0.665
BL1-6-4	0.05572	0.78	0.54917	1.70	0.0715	1.50	441.0	17.3	444.5	6.1	445.1	6.5	272	232	0.852
BL1-6-5	0.05659	0.61	0.58620	1.63	0.0751	1.51	475.6	13.3	468.4	6.1	467.0	6.8	493	199	0.404
BL4-5 Granite aplite; Concordia age = 270 ± 2 Ma (MSWD = 0.06)															
BL4-5-1	0.05224	0.71	0.30428	1.72	0.0427	1.52	272.9	18.3	269.7	4.1	269.4	4.0	590	175	0.296
BL4-5-2	0.05227	0.57	0.30343	1.65	0.0426	1.53	269.7	14.3	269.1	3.9	269.0	4.0	1406	447	0.318
BL4-5-3	0.05200	1.01	0.30241	1.83	0.0424	1.50	271.4	23.8	268.3	4.3	267.9	3.9	720	114	0.158
BL4-5-4	0.05156	0.51	0.31005	1.59	0.0436	1.50	265.8	11.8	274.2	3.8	275.2	4.0	1136	263	0.231
BL4-5-5	0.05146	0.57	0.31102	1.60	0.0438	1.50	261.5	12.9	275.0	3.9	276.6	4.1	978	374	0.383
BL4-5-6	0.05165	0.56	0.30457	1.61	0.0428	1.51	270.1	12.9	270.0	3.8	269.9	4.0	945	178	0.189
BL4-5-7	0.05185	0.78	0.30380	1.71	0.0427	1.50	268.2	18.6	269.4	4.0	269.5	4.0	790	215	0.272
BL4-5-8	0.05215	0.64	0.30230	1.66	0.0422	1.51	283.2	15.3	268.2	3.9	266.5	4.0	710	128	0.181
BL4-5-9	0.05210	0.44	0.30911	1.57	0.0433	1.50	275.7	10.5	273.5	3.8	273.2	4.0	2504	1318	0.526
BL4-5-10	0.05186	0.61	0.30728	1.64	0.0430	1.52	279.3	13.9	272.1	3.9	271.2	4.0	797	142	0.179
BL4-5-11	0.05182	0.64	0.30718	1.63	0.0430	1.50	277.4	14.5	272.0	3.9	271.4	4.0	879	258	0.294
BL4-5-12	0.05185	0.78	0.30866	1.70	0.0432	1.51	277.2	17.9	273.1	4.1	272.7	4.0	1313	287	0.218
BL4-5-13	0.05205	0.47	0.30847	1.60	0.0430	1.53	287.8	10.7	273.0	3.8	271.3	4.1	1310	486	0.371
BL4-5-14	0.05168	1.00	0.30777	1.80	0.0432	1.50	271.2	22.8	272.5	4.3	272.6	4.0	762	122	0.161
BL4-5-15	0.05143	0.62	0.30453	1.62	0.0429	1.50	260.1	14.1	269.9	3.9	271.1	4.0	1051	265	0.253
BL4-5-16	0.05201	0.78	0.30770	1.72	0.0433	1.50	265.6	19.3	272.4	4.1	273.2	4.0	903	200	0.222
BL4-5-17	0.05190	0.60	0.30359	1.62	0.0424	1.50	281.0	13.7	269.2	3.8	267.8	3.9	972	248	0.255
BL4-5-18	0.05208	0.89	0.30375	1.74	0.0423	1.50	288.8	20.2	269.3	4.1	267.1	3.9	878	237	0.270
BL4-5-19	0.05193	0.63	0.30658	1.65	0.0429	1.51	275.8	15.0	271.5	3.9	271.0	4.0	733	121	0.165
BL4-5-20	0.05225	1.06	0.30317	1.87	0.0422	1.51	289.5	25.0	268.9	4.4	266.5	3.9	276	150	0.545

(*continued on next page*)

Table 2 (*continued*)

Sample No.	Ratio						Model age						U-Th		
	$^{207}Pb/^{206}Pb$	1σ (%)	$^{207}Pb/^{235}U$	1σ (%)	$^{206}Pb/^{238}U$	1σ (%)	$^{207}Pb/^{206}Pb$	1σ	$^{207}Pb/^{235}U$	1σ	$^{206}Pb/^{238}U$	1σ	U (ppm)	Th (ppm)	Th/U
BL4-5-21	0.05187	0.44	0.30599	1.56	0.0428	1.50	278.0	10.1	271.1	3.7	270.3	4.0	1516	450	0.297
BL4-5-22	0.05186	0.93	0.30593	1.83	0.0429	1.57	275.7	21.4	271.0	4.4	270.5	4.2	835	308	0.369
BL4-5-23	0.05183	0.60	0.30412	1.62	0.0426	1.50	278.1	13.7	269.6	3.8	268.6	3.9	819	147	0.179
BL4-5-24	0.05172	0.53	0.30382	1.60	0.0426	1.51	270.7	12.3	269.4	3.8	269.2	4.0	1178	286	0.242

Sample No.	Hf isotope								Oxygen isotope	
	$^{176}Yb/^{177}Hf$	$^{176}Lu/^{177}Hf$	$^{176}Hf/^{177}Hf$	2σ	$e_{Hf}(t)$	2σ	$f_{Lu/Hf}$	$T_{DM1}(Hf)$	$T_{DM2}(Hf)$	$\delta^{18}O$ (‰)	2σ
BL1-6 Granodiorite porphyry; Concordia age = 269 ± 2 Ma (MSWD = 0.4)											
BL1-6-1	0.0199	0.0006	0.282780	18	6.1	0.6	-0.98	662	778	6.97	0.17
BL1-6-2	0.0243	0.0008	0.282772	20	5.8	0.7	-0.98	676	795	6.99	0.27
BL1-6-3	0.0237	0.0007	0.282815	18	7.3	0.6	-0.98	615	716	7.04	0.24
BL1-6-4	0.0222	0.0007	0.282823	19	7.6	0.7	-0.98	603	701	7.05	0.22
BL1-6-5											
BL1-6-6											
BL1-6-7											
BL1-6-8											
BL1-6-9	0.0250	0.0008	0.282783	18	6.2	0.6	-0.98	661	775	7.23	0.18
BL1-6-10	0.0206	0.0006	0.282803	18	6.9	0.6	-0.98	630	738	7.63	0.19
BL1-6-11	0.0222	0.0007	0.282834	19	8.0	0.7	-0.98	587	681	7.40	0.19
BL1-6-12	0.0682	0.0022	0.282934	20	11.3	0.7	-0.94	465	513	7.07	0.11
BL1-6-13	0.0258	0.0008	0.282809	22	7.1	0.8	-0.98	624	728	7.18	0.21
BL1-6-14	0.0215	0.0007	0.282765	17	5.5	0.6	-0.98	685	807	6.85	0.38
BL1-6-15	0.0231	0.0007	0.282803	17	6.9	0.6	-0.98	631	738		
BL1-6-16	0.0153	0.0005	0.282755	19	5.2	0.7	-0.99	694	823	6.98	0.25
BL1-6-17											
BL1-6-18	0.0239	0.0007	0.282804	21	6.9	0.7	-0.98	631	737	7.03	0.21
BL1-6 Core domain; Concordia age = 445 ± 6 Ma (MSWD = 1.3)											
BL1-6-1	0.0241	0.0009	0.282591	16	3.1	0.6	-0.97	933	1074	6.57	0.17
BL1-6-2	0.0410	0.0014	0.282701	19	6.9	0.7	-0.96	790	883	7.33	0.21
BL1-6-3	0.0376	0.0013	0.282628	25	4.3	0.9	-0.96	891	1012	7.01	0.13
BL1-6-4	0.0244	0.0009	0.282596	19	3.3	0.7	-0.97	927	1065	6.20	0.17
BL1-6-5	0.0327	0.0011	0.282451	20	-1.9	0.7	-0.97	1136	1329	6.47	0.23
BL4-5 Granite aplite; Concordia age = 270 ± 2 Ma (MSWD = 0.06)											
BL4-5-1	0.0024	0.0001	0.282666	18	2.2	0.6	-1.00	809	980	6.72	0.3
BL4-5-2	0.0164	0.0005	0.282740	16	4.7	0.6	-0.99	715	850	7.23	0.2
BL4-5-3	0.0200	0.0006	0.282766	19	5.6	0.7	-0.98	680	803	7.28	0.3
BL4-5-4	0.0140	0.0004	0.282669	20	2.2	0.7	-0.99	813	978	7.32	0.2
BL4-5-5											
BL4-5-6											
BL4-5-7											
BL4-5-8	0.0082	0.0002	0.282705	17	3.5	0.6	-0.99	759	910	7.19	0.2
BL4-5-9											
BL4-5-10											
BL4-5-11	0.0235	0.0007	0.282735	20	4.5	0.7	-0.98	727	861	7.11	0.3
BL4-5-12											
BL4-5-13	0.0136	0.0004	0.282740	18	4.7	0.6	-0.99	715	850	6.92	0.2
BL4-5-14	0.0173	0.0005	0.282763	20	5.5	0.7	-0.98	684	808	7.40	0.3

(*continued on next page*)

Table 2 (*continued*)

Sample No.	Hf isotope								Oxygen isotope	
	$^{176}Yb/^{177}Hf$	$^{176}Lu/^{177}Hf$	$^{176}Hf/^{177}Hf$	2σ	$\varepsilon_{Hf}(t)$	2σ	$f_{Lu/Hf}$	$T_{DM1}(Hf)$	$T_{DM2}(Hf)$	$\delta^{18}O$ (‰)	2σ
BL4-5-15	0.0189	0.0006	0.282665	21	2.0	0.7	-0.98	823	988	7.34	0.2
BL4-5-16	0.0096	0.0003	0.282713	17	3.8	0.6	-0.99	750	897	7.10	0.2
BL4-5-17	0.0164	0.0005	0.282684	20	2.7	0.7	-0.98	795	952	7.36	0.2
BL4-5-18	0.0188	0.0006	0.282734	25	4.5	0.9	-0.98	727	863	7.36	0.2
BL4-5-19	0.0218	0.0007	0.282755	24	5.2	0.9	-0.98	698	825	7.28	0.3
BL4-5-20	0.0266	0.0008	0.282762	28	5.5	1.0	-0.98	690	812	7.36	0.3
BL4-5-21											
BL4-5-22											
BL4-5-23											
BL4-5-24	0.0142	0.0004	0.282651	24	1.6	0.9	-0.99	838	1011	7.2	0.2

gold are secondary rather than primary, and thus, the reserve of this "gold core" should be overestimated. Moreover, the potassic alteration is developed in the deep part, forming secondary biotite and K-feldspar (see Appendix A), and usually overprinted by the later alterations. These features are typical of general porphyry Cu–Au–Mo deposits. On the whole, the Bilihe deposit is supposed to be a porphyry Au deposit and more attention should be paid to the formation process of magmatic Au as Yang et al. (2015) considered.

Supplementary data associated with this article can be found, in the online version, at https://doi.org/10.1016/j.jseaes.2018.07.016.

Porphyry gold deposits as a special and potentially economic gold type have attracted considerable attention. In general, Miocene is the dominant period for porphyry gold deposits. For the Bilihe deposit, the porphyry orebody II occurs in the inner contact zones of porphyry intrusions and is characterized mainly by net vein mineralization, with minor dendritic, agglomerated auriferous quartz. In the open pit, two types of intrusions have been identified, including granodiorite and granite aplite, both of which have been cut across by the auriferous quartz veins. Hence, the crystallization age of 269 Ma of these intrusions represents the upper limit of gold mineralization. Meanwhile, molybdenite veins crosscut these intrusions and various auriferous quartz veins and thus, the molybdenite Re–Os ages suggest that precipitation of gold was older than 268 Ma. Therefore, the gold mineralization age of the Bilihe deposit can be constrained at ca. 269 Ma.

Both zircon Hf and O isotopes are useful tools to trace the magma source. Because zircon has very low Lu/Hf ratios (commonly < 0.002) and virtually negligible $^{176}Hf/^{177}Hf$ isotopes due to ^{176}Lu decay, zircon roughly preserves the initial $^{176}Hf/^{177}Hf$ ratio inherited from the magma at the time of formation (Patchett et al., 1982; Wu et al., 2007). Oxygen isotopes have been extensively employed to trace magma sources and constrain the history of mixing with crustal material. Magmas with no crustal input generally have uniform oxygen isotopes that are distinct from magmas that assimilated or were generated directly from crustal sources.

The zircon ε_{Hf} (t) values of granite aplite (1.6–5.6) and granodiorite (5.2–11.3) is suggestive of the involvement of older crust to mantle-derived magmas. It should be noted that ε_{Hf} (t) values of the former are more evolved than the latter, suggesting a greater input of a crustal component to the magmatism. Moreover, the higher $\delta^{18}O$ values of 6.20–7.63‰ relative to the mantle also reflect a contribution of crustal material involved (Fig. 8a). Furthermore, the Hf–O isotope correlations may be plausibly explained by the mixing of components between the continental crust and mantle materials. In the $\delta^{18}O$ vs. ε_{Hf} (t) diagram (Fig. 8b), the samples lie on a mixing line between MORB and ancient continental crust end members, showing that continental crust and depleted mantle contributed ~50% of the zircon Hf and O isotope values, respectively. Therefore, the Bilihe magma was likely generated by partial melting of the metasomatized mantle coupled with the assimilation of crustal materials (such as the Bainaimiao Group) during its ascending.

It has been accepted that in the Central Asian Metallogenic Domain (CAMD), there are multiple porphyry metallogenic events occurring between 500 and 100 Ma, likely due to the subduction of the Paleo-Asian and Paleo-Pacific oceanic slabs and the destruction of the North China Craton (Gao et al., 2017 and references therein). In the $\delta^{18}O$ vs. ε_{Hf} (t) diagram, including data from other mineralized porphyries in the CAMD (Fig. 8a), it can be seen that much mantle material was involved in the Cu–Au–Mo mineralization in the western CAMD, whereas in the eastern to northeastern CAMD, older crustal contamination played an increasingly important role in Cu–Mo-related magma. This difference may imply that from west to east in the CAMD, more microcontinent blocks were involved in the accretionary orogenic processes and the metallogenic events.

Thus far, whether the late Permian represents the timing of the final closure of the Paleo-Asian Ocean is still controversial (Xiao et al., 2003; Zhang et al., 2009b and references therein). Based on geochemical

Table 3
Molybdenite Re-Os isotopic results of the Bilihe gold deposit.

Sample	Weight (g)	Re (ppm)	1σ	^{187}Re (ppm)	1σ	^{187}O (ppb)	1σ	Age (Ma)	1σ
B-Mo-101	0.00032	1984	18	1247	11	5578	36	268	4
B-Mo-06	0.00697	202	2	127	1	574	4	271	4
B-Mo-06-1	0.00305	199	2	125	1	562	5	270	4
B-Mo-08	0.00017	1635	11	1027	7	4606	31	269	4
B-Mo-401	0.00044	2408	32	1514	20	6735	60	267	5
B-Mo-402	0.00060	2570	27	1615	17	7179	56	266	4
B-Mo-403	0.00023	740	6	465	4	2076	13	267	4
B-Mo-404	0.00025	3795	38	2385	24	10,744	71	270	4
B-Mo-405	0.00024	2148	16	1350	10	6022	39	267	4

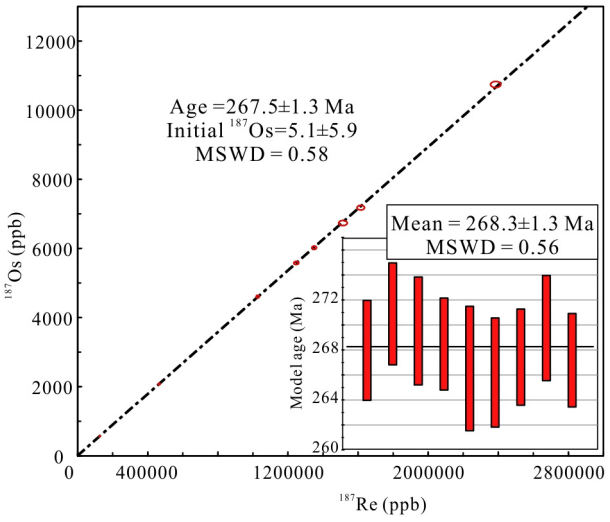

Fig. 7. Molybdenite Re–Os isochron and weighted mean plots of model ages (insert) from the Bilihe deposit.

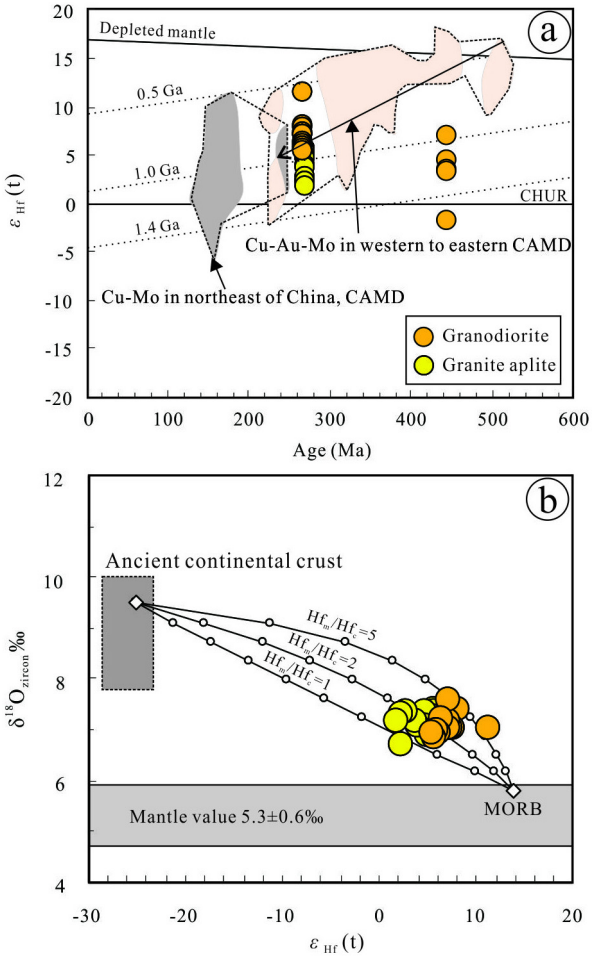

Fig. 8. Zircon age vs. ε_{Hf} (t) (a) and ε_{Hf} (t) vs. $\delta^{18}O$ diagrams (b). a–showing Hf–O data of porphyry Cu–Au–Mo deposits in the central Asian metallogenic domain (CAMD), compiled from Gao et al. (2017). Mantle $\delta^{18}O$ value of 5.3 ± 0.6‰ is after Valley et al. (1998).

characteristics of the porphyry intrusions at the Bilihe deposit, Liu and Nie (2015) favored a late stage of closure of the Paleo-Asian Ocean, whereas Yang et al. (2016) employed a southward subduction setting to interpret the formation of the Bilihe intrusions. By comparison with formation settings where other porphyry Au deposits were formed in worldwide, it is noted that a series of gold mineralization in the Maricunga belt was followed immediately by periods of crustal thickening associated with the dramatic tectonic changes as the Nazca plate subduction in the Central Andes (Vila and Sillitoe, 1991; Kay et al., 1994; Muntean and Einaudi, 2000), and that Harangi et al. (2007) considered that the magmas ponded beneath the thick continental crust and initiated melting in the lower crust accounting for the formation of the Javorie ore-related porphyry in Slovakia. Therefore, it seems that porphyry gold deposits favor a thickened crustal setting. This crustal thickening model related to the collisional intermission of the Paleo-Asian Ocean should also be useful to interpret the formation setting of the Bilihe deposit, as well as the evidence of captured older zircons and Hf–O isotopes, which imply older crustal contamination taking part in the Bilihe gold mineralization.

7. Conclusion

This study demonstrates that the isotopic dating of porphyry gold mineralization can place constraints on the ore genesis. The Zircon U–Pb ages of the granodiorite porphyry and granite aplite indicate that the gold mineralization was younger than 269 Ma. Molybdenite from later molybdenite veins has a Re–Os age of 268 Ma. Hence, the porphyry gold mineralization can be precisely constrained at ca. 269 Ma. Hf–O isotopes show that the ore-forming magmas were derived from partial melting of the metasomatized mantle coupled with extensive contamination by recycled crustal materials.

Acknowledgments

The authors are grateful to Tianzhu Ye and the mining geologists of Bilihe Mining Company for their help during field works. Comments from Ph.D. Changle Wang and two anonymous reviewers have given a

great improvement for the paper. This work is supported by the National Natural Science Foundation of China (Nos. 41390445, 41572073 and 41503056), the National Key R&D Program of China (Grant No. 2016YFC0600106) and State Key Laboratory of Ore Deposit Geochemistry Opening Fund (201501).

References

Bai, W., Qin, M., 2012. Research report of Bilihe gold deposit in Sonid Right Banner, Inner Mongolia. In: Bai, W., Qin, M. (Eds.). Gold Geological Institute of CPPF, p. 268 (in Chinese).

Gamonal, S., 2015. Volcanic Stratigraphy and Epithermal Mineralization of the La Coipa District, Maricunga belt. University of British Columbia, Chile.

Gao, J., Klemd, R., Zhu, M., Wang, X., Li, J., Wan, B., Xiao, W., Zeng, Q., Shen, P., Sun, J., Qin, K., Campos, E., 2017. Large-scale porphyry-type mineralization in the Central Asian metallogenic domain: a review. J. Asian Earth Sci. https://doi.org/10.1016/j.jseaes.2017.10.002.

Ge, L., Qing, M., Yuan, S., Tang, M., Xing, J., 2009. Prospecting process of Bilihe large-sized gold deposit in Inner Mongolia and its revelatory significance. Mineral Deposits 28, 390–402 (in Chinese with English abstract).

Gil-Rodríguez, J., 2010. Igneous Petrology of the Colosa Gold-rich Porphyry System (Tolima, Colombia). University of Arizona. p. 51.

Hanes, R., Bakos, F., Fuchs, P., Žitňan, P., Konečný, V., 2010. Exploration results of Au porphyry mineralizations in the Javorie stratovolcano. Mineralia Slovaca 42, 15–32.

Harangi, S., Downes, H., Thirlwall, M., Gméling, K., 2007. Geochemistry, petrogenesis and geodynamic relationships of Miocene calc-alkaline volcanic rocks in the Western Carpathian arc, eastern central Europe. J. Petrol. 48, 2261–2287.

Harris, A.C., Kamenetsky, V.S., White, N.C., Steele, D.A., 2004. Volatile phase separation in silicic Magmas at Bajo de la Alumbrera porphyry Cu-Au deposit, NW Argentina. Resour. Geol. 54, 341–356.

Jin, X., Li, W., Xiang, P., Sakyi, P.A., Zhu, M., Zhang, L., 2013. A contribution to common Carius tube distillation techniques. J. Anal. Atomic Spectrom. 28, 396–404.

Jin, X.D., Li, W.J., Wu, H.Y., Zhang, L.C., Du, A.D., 2010. Development of Re–Os isotopic dating analytical technique and determination know-how on ICP-MS precise dating for molybdenite. Acta Petrologica Sinica 26, 1617–1624 (in Chinese with English abstract).

Kay, S.M., Mpodozis, C., Tittler, A., Cornejo, P., 1994. Tertiary magmatic evolution of the Maricunga mineral belt in Chile. Int. Geol. Rev. 36, 1079–1112.

Koděra, P., Heinrich, C.A., Wälle, M., Lexa, J., 2014. Magmatic salt melt and vapor: extreme fluids forming porphyry gold deposits in shallow subvolcanic settings. Geology 42, 495–498.

Kröner, A., Kovach, V., Belousova, E., Hegner, E., Armstrong, R., Dolgopolova, A., Seltmann, R., Alexeiev, D.V., Hoffmann, J.E., Wong, J., Sun, M., Cai, K., Wang, T., Tong, Y., Wilde, S.A., Degtyarev, K.E., Rytsk, E., 2014. Reassessment of continental growth during the accretionary history of the Central Asian Orogenic Belt. Gondwana Res. 25, 103–125.

Li, J., Zhang, J., Yang, T., Li, Y., Sun, G., Zhu, Z., Wang, L., 2009. Crustal tectonic division and evolution of the southern part of the north Asian orogenic region and its adjacent areas. J. Jilin University (Earth Science Edition) 584–605 (in Chinese with English abstract).

Li, Q.L., Li, X.H., Liu, Y., Tang, G.Q., Yang, J.H., Zhu, W.G., 2010a. Precise U-Pb and Pb–Pb dating of Phanerozoic baddeleyite by SIMS with oxygen flooding technique. J. Anal. Atomic Spectrom. 25, 1107–1113.

Li, W., Zhong, R., Xu, C., Song, B., Qu, W., 2012. U-Pb and Re–Os geochronology of the Bainaimiao Cu–Mo–Au deposit, on the northern margin of the North China Craton, Central Asia Orogenic Belt: implications for ore genesis and geodynamic setting. Ore Geol. Rev. 48, 139–150.

Li, X., Tang, G., Gong, B., Yang, Y., Hou, K., Hu, Z., Li, Q., Liu, Y., Li, W., 2013. Qinghu zircon: a working reference for microbeam analysis of U-Pb age and Hf and O isotopes. Chinese Sci. Bull. 58, 4647–4654.

Li, X.H., Long, W.G., Li, Q.L., Liu, Y., Zheng, Y.F., Yang, Y.H., Chamberlain, K.R., Wan, D.F., Guo, C.H., Wang, X.C., 2010b. Penglai zircon megacrysts: a potential new working reference material for microbeam determination of Hf–O isotopes and U–Pb age. Geostandards Geoanal. Res. 34, 117–134.

Liu, C., Nie, F., 2015. Permian magmatic sequences of the Bilihe gold deposit in central Inner Mongolia, China: petrogenesis and tectonic significance. Lithos 231, 35–52.

Liu, J., Wu, G., Li, T., Wang, G., Wu, H., 2014. SHRIMP zircon U-Pb dating, geochemistry, Sr-Nd isotopic analysis of the Late Paleozoic intermediate-acidic intrusive rocks in the Hadamiao area, Xianghuang Banner, Inner Mongolia and its geological significances. Acta Petrologica Sinica 30, 95–108 (in Chinese with English abstract).

Lu, Y., Li, W., Lai, Y., 2009. Time and tectonic setting of hosting porphyry of the Hadamiao gold deposit in Xianghuangqi, Inner Mongolia. Acta Petrologica Sinica 25, 2615–2620 (in Chinese with English abstract).

Lu, Y., Pan, M., Qing, M., Zhang, Y., Han, X., Chao, Y., 2012. Zircon U-Pb age of gold-bearing granitic intrusive rocks in Bilihe gold deposit of Inner Mongolia and its geological significance. Acta Petrologica Sinica 28, 993–1004 (in Chinese with English abstract).

Ludwig, K.R., 2003. ISOPLOT 3.0-a geochronological toolkit for Microsoft Excel, Berkeley Geochronology Center Special. Publication 70.

Muntean, J.L., Einaudi, M.T., 2000. Porphyry gold deposits of the Refugio District, MaricungaBelt, Northern Chile. Econ. Geol. 95, 1445–1472.

Muntean, J.L., Einaudi, M.T., 2001. Porphyry-epithermal transition: Maricunga Belt, Northern Chile. Econ. Geol. 96, 743–772.

Nie, F., Pei, R., Wu, L., Bjorlykke, A., 1994a. Sm-Nd isotope study on Late Paleozoic volcanic rocks of Bieluwutu formation Inner Mongolia. Acta Petrologica ET Mineralogica 289–296 (in Chinese with English abstract).

Nie, F., Pei, R., Wu, L., Bjorlykke, A., 1995. Nd-and Sr-isotope study on greenschist and granodiorite of the Bainaimiao district, Inner Mongolia, China. Acta Geoscientia Sinica 1, 36–44 (in Chinese with English abstract).

Nie, F., Pei, R., Wu, L., Bjørlykke, A., 1994b. Nd, Sr and Pb isotopic study of copper (gold) and gold deposits in Bainaimiao area. Inner Mongolia. Miner. Depos. 13, 331–344 (in Chinese with English abstract).

Patchett, P.J., Kouvo, O., Hedge, C.E., Tatsumoto, M., 1982. Evolution of continental crust and mantle heterogeneity: evidence from Hf isotopes. Contrib. Mineral. Petrol. 78, 279–297.

Qin, M., Tang, G.J., Ge, L., Han, X., Feng, J., Yuan, W., Zhao, Y., 2012. La-ICP-MS zircon U-Pb age, geochemistry of andesite in Bilihe goldfield, Suniteyouqi, Inner Mongolia and its tectonic significance. Acta Petrologica Sinica 28, 514–524.

Qing, M., Ge, L., Tang, W., Yuan, S., Zhao, Y., 2011. Molybdnite Re-Os isotope age of Bilihe large-size porphyry gold deposit in Sunid Right Banner of Inner Mongolia and its geological significance. Mineral Depos. 30, 11–20 (in Chinese with English abstract).

Richards, J.P., 2009. Postsubduction porphyry Cu-Au and epithermal Au deposits: products of remelting of subduction-modified lithosphere. Geology 37, 247–250.

Santacruz Reyes, L., 2016. Caracterização petrológica e metalogenética do depósito de Au de Marmato. Manizales, Colômbia.

Sengör, A., Natal'In, B., Burtman, V., 1993. Evolution of the Altaid tectonic collage and Palaeozoic crustal growth in Eurasia. Nature 364, 22.

Sillitoe, R.H., 1979. Some thoughts on gold-rich porphyry copper deposits. Mineralium Deposita 14, 161–174.

Sillitoe, R.H., 2008. Special paper: major gold deposits and belts of the North and South American Cordillera: distribution, tectonomagmatic settings, and metallogenic considerations. Econ. Geol. 103, 663–687.

Sillitoe, R.H., 2010. Porphyry copper systems. Econ. Geol. 105, 3–41.

Sillitoe, R.H., McKee, E.H., Vila, T., 1991. Reconnaissance K-Ar geochronology of the Maricunga gold-silver belt, northern Chile. Econ. Geol. 86, 1261–1270.

Szabó, C., Harangi, S., Csontos, L., 1992. Review of Neogene and Quaternary volcanism of the Carpathian-Pannonian region. Tectonophysics 208, 243–256.

Tang, K., Yan, Z., 1993. Regional metamorphism and tectonic evolution of the Inner Mongolian suture zone. J. Metamorphic Geol. 11, 511–522.

Valley, J.W., Kinny, P.D., Schulze, D.J., Spicuzza, M.J., 1998. Zircon megacrysts from kimberlite: oxygen isotope variability among mantle melts. Contrib. Mineral. Petrol. 133, 1–11.

Vila, T., Sillitoe, R.H., 1991. Gold-rich porphyry systems in the Maricunga Belt, northern Chile. Econ. Geol. 86, 1238–1260.

Vila, T., Sillitoe, R.H., Betzhold, J., Viteri, E., 1991. The porphyry gold deposit at Marte, northern Chile. Econ. Geol. 86, 1271–1286.

Windley, B.F., Alexeiev, D., Xiao, W., Kröner, A., Badarch, G., 2007. Tectonic models for accretion of the Central Asian Orogenic Belt. J. Geol. Soc. 164, 31–47.

Woodhead, J., Hergt, J., Shelley, M., Eggins, S., Kemp, R., 2004. Zircon Hf-isotope analysis with an excimer laser, depth profiling, ablation of complex geometries, and concomitant age estimation. Chem. Geol. 209, 121–135.

Wu, F.-Y., Yang, Y.-H., Xie, L.-W., Yang, J.-H., Xu, P., 2006. Hf isotopic compositions of the standard zircons and baddeleyites used in U-Pb geochronology. Chem. Geol. 234, 105–126.

Wu, F., Li, X., Zheng, Y., Gao, S., 2007. Lu–Hf isotopic systematics and their applications in petrology. Acta Petrologica Sinica 23, 185–220 (in Chinese with English abstract).

Xiao, W., Windley, B.F., Hao, J., Zhai, M., 2003. Accretion leading to collision and the Permian Solonker suture, Inner Mongolia, China: termination of the central Asian orogenic belt. Tectonics 22.

Yang, Z., Chang, Z., Hou, Z., Meffre, S., 2016. Age, igneous petrogenesis, and tectonic setting of the Bilihe gold deposit, China, and implications for regional metallogeny. Gondwana Res. 34, 296–314.

Yang, Z., Chang, Z., Paquette, J., White, N.C., Hou, Z., Ge, L., 2015. Magmatic Au mineralization at the Bilihe Au deposit, China. Econ. Geol. 110, 1661–1668.

Zhang, S.-H., Zhao, Y., Kröner, A., Liu, X.-M., Xie, L.-W., Chen, F.-K., 2009a. Early Permian plutons from the northern North China Block: constraints on continental arc evolution and convergent margin magmatism related to the Central Asian Orogenic Belt. Int. J. Earth Sci. (Geol Rundsch) 98, 1441–1467.

Zhang, S.-H., Zhao, Y., Song, B., Hu, J.-M., Liu, S.-W., Yang, Y.-H., Chen, F.-K., Liu, X.-M., Liu, J., 2009b. Contrasting Late Carboniferous and Late Permian-Middle Triassic intrusive suites from the northern margin of the North China craton: geochronology, petrogenesis, and tectonic implications. Geol. Soc. Am. Bull. 121, 181–200.